Journal of Materials Chemistry C

ROYAL SOCIETY OF CHEMISTRY

PAPER

View Article Online
View Journal | View Issue

Cite this: J. Mater. Chem. C, 2026, 14, 5934

Quasi-one-dimensional magnetism of transition-metal oxide in Fe-based inorganic–organic hybrid nanosheets

Takayuki Nakane, *[a] Takashi Naka,[ba] Kazuyoshi Sato,[c] Noriki Terada,[a] Pascal Manuel,[d] Ahmed Ibrahim,[e] Shiro Kubuki,[e] Chiya Numako,[f] Dimitry Khalyavin,[d] Anne de Visser[g] and Hiroya Abe[h]

Received 22nd October 2025,
Accepted 8th February 2026

DOI: 10.1039/d5tc03791c

rsc.li/materials-c

Low dimensionality provides an exciting research field for investigating quantum effects in functional materials. This work reports a novel quasi one-dimensional (1D) spin system configured in an inorganic–organic hybrid nanosheet. This nanosheet was solvothermally synthesized from $FeCl_3$, CH_3COOK, and ethylene glycol ($C_2H_6O_2$) as the solvent. The minimum chemical composition of this hybrid nanosheet is $Fe_7O_{4.77}(C_2H_4O_2)_9$, and the quantum magnetic properties arise from a quasi-1D spin system of Fe^{3+}. Remarkably, this quasi-1D antiferromagnetism exhibits a critical temperature at 21 K, implying a relatively low magnetic fluctuation state compared with an ideal 1D spin system. The unique characteristics of this novel inorganic–organic hybrid nanosheet are therefore considered attractive for tailoring novel low-dimensional quantum devices.

1. Introduction

Low-dimensional materials provide an exciting research platform for investigating functional quantum phenomena,[1–9] such as superconductivity,[1,2] metal–insulator transitions,[3] and multistage magnetic ordering.[4] The unique characteristics and potential of one-dimensional (1D) materials were actively predicted in the early stages of modern materials science.[10–14] However, the fabrication of 1D materials and the detection of their distinctive features were challenging, although recent advances in nanotechnology have drastically boosted this research field.

Quantum properties generally arise in nanoscale regions. Consequently, the functional signal from an individual quantum region is typically weak. Therefore, the effective alignment of quantum regions to bundle these weak responses is of paramount importance for investigating the functionality of 1D materials. To address this issue, fabrication techniques of hybrid nanomaterials have recently come to the fore as effective approaches to tailor novel quantum materials.[15–18] A hybrid nanomaterial is generally defined as a compound consisting of a nanostructured matrix within a framework of organic molecules.[19,20] Thus, it is not a simple mixture of components; rather, the constituents form an original crystal structure through chemical bondings.

Here, we report the discovery of a novel hybrid material in a precursor nanosheet used for synthesizing shape-controlled Fe_3O_4 microcrystals.[21] The uniqueness of this hybrid nanosheet resides in its quasi-1D properties, displaying a phase transition that originates from the distinctive structure of the iron oxide within the material. The crystal structure remains to be clarified. This work precisely characterizes this novel hybrid nanosheet involving a quasi-1D spin system of Fe^{3+} (HNS-1DFe).

[a] National Institute for Materials Science, 1-2-1, Sengen, Tsukuba, Ibaraki 305-0047, Japan
[b] University of the Ryukyus, 1 Senbaru, Nishihara-cho, Nakagami-gun, Okinawa 903-0213, Japan
[c] Gunma University, 1-5-1 Tenjin-cho, Kiryu, Gunma 376-8515, Japan
[d] ISIS Facility, STFC Rutherford Appleton Laboratory, Chilton, Didcot, Oxfordshire, OX11 0QX, UK
[e] Tokyo Metropolitan University, 1-1 Minami-Osawa, Hachi-Oji, Tokyo 192-0397, Japan
[f] Graduate School of Science, Chiba University, Chiba 263-8522, Japan
[g] University of Amsterdam, Science Park 904, 1098 XH, The Netherlands
[h] Osaka University, 11-1 Mihogaoka, Ibaraki, Osaka 567-0047, Japan

2. Experiments

2.1. Synthesis and fundamental characterization

HNS-1DFe was solvothermally synthesized from 0.5 M $FeCl_3$ (96.0%, Kanto Chemical: Japan) and 3 M CH_3COOK (97.0%, Kishida Chemical: Japan) in dehydrated anhydrous ethylene glycol (EG: 99.8%, Sigma-Aldrich: USA) as the solvent.[21] These solutions were mixed, sealed into a reaction tube with a high allowable inner pressure, and heated at 180 °C for 2 h in an oil bath. After synthesis, the product was extracted, washed three

times with EG using centrifugation under 10 000 G for 10 min, and finally dried for 1 week. This fabrication procedure reproducibly yielded a dark yellow nanosheet powder; however, the colour was slightly different among samples synthesized on different days. Therefore, all evaluations in this study were conducted using a single sample batch to maintain consistency in the discussion.

The chemical composition of the product HNS-1DFe was evaluated by inductively coupled plasma optical emission spectroscopy (ICP-OES: Ultima-2, HORIBA: Japan) and organic elemental analysis (OEA: TruSpec Micro CHN, LECo: USA). Tht thermal stability of HNS-1DFe was verified by thermogravimetric analysis (TG: TGD-7000RH/SP, ULVAC: Japan) under flowing N_2.

2.2. Morphology and structural characterizations

The morphology of HNS-1DFe was observed by field-emission scanning electron microscopy (FE-SEM: SU-8000, Hitachi High-Tech: Japan), and the crystal structure was verified from field-emission transmission electron microscopy (FE-TEM: JEM-2000F, Japan Electron: Japan) images acquired with an accelerating voltage of 200 kV.

Spectroscopic structural analysis was also carried out using Fourier transform infrared spectroscopy (FT-IR: FT/IR-680 Plus, JASCO: Japan) with the specimen prepared as KBr pellets, and Raman spectroscopy (NanoFinder-1000, Tokyo Instrument: Japan) with a 532 nm excitation laser, respectively. The powder X-ray diffraction (XRD) pattern was measured using a conventional diffractometer (MiniFlex-600, RIGAKU: Japan) with copper K_α radiation. Powder Neutron diffraction (PND) measurements were conducted on a long-wavelength diffractometer (WISH, ISIS Neutron and Muon Source: UK), which covers long d-spacing values up to 100 Å in magnetic and large unit-cell systems.[22]

The main valence state of iron ions and their cationic configurations in HNS-1DFe were also evaluated by Fe K-edge X-ray absorption fine structure (XAS) spectra measured at BL-9A, photon factory, KEK, Japan, using the transmission method. Data processing of the X-ray absorption near-edge structure (XANES) region and extended X-ray absorption fine structure (EXAFS) region in the XAS spectra was carried out using the data processing program, ATHENA.[23] Measurements of ^{57}Fe Mössbauer spectra were carried out under constant acceleration mode. A γ-ray source of ^{57}Co(Rh) (1.85 GBq, MCo7.124/74/20, Rietverc, verified on 02.12. 2020) was attached to the transducer, and α-Fe (30 μm thickness, MRA 2.6/30.20) was used as a reference for zero-velocity and velocity-scale calibration, with the sample placed in front of the proportional counter (45431, Niki-Kogei). For the measurements, 40 mg of the well-pulverized sample was shaped into a 10 mm diameter pellet and fixed on cellophane tape. The γ-ray from the source through the sample was detected by the proportional counter under an applied voltage of 2 kV supplied by a high-voltage power supply (556, ORTEC: USA).

2.3. Measurement of physical properties

The physical properties of HNS-1DFe were characterized in terms of dc-magnetization and specific heat by using a Magnetic Properties Measurement System (MPMS-XL, Quantum Design: USA) and a Physical Properties Measurement System (PPMS Dynacool, Quantum Design: USA), respectively. The magnetic contribution of Fe^{3+} ions in the specific heat, C_{mag}, was estimated as $C_{mag}/T = [C_{mol} - C_{lattice}]/T$ for HNS-1DFe. Here, $C_{lattice}$ denotes the lattice contribution to the specific heat, and the estimation procedure is given in the SI (SI-4). Then, the magnetic entropy, $S_{mag}(T)$, was calculated as follows.

$$S_{mag}(T) = \int_{T_{min}}^{T} \frac{C_{mag}}{T} dT \quad (1)$$

here, $T_{min} \approx 1.9$ K is the lowest experimental temperature. On the other hand, the temperature dependence of C_{mag}, $C_{mag}(T)$, followed the power law $C_{mag} = \delta'' T^{\alpha}$ ($\alpha \approx 3$),[24] and $C_{mag}(T)$ was fit to determine the δ'' and α values. The δ'' serves as a prefactor. The exponent α is discussed as d_{mag}/n, where d_{mag} is the dimension of the spin system and n is an index indicating ferromagnetic ($n = 2$) or AF ($n = 1$) interactions between spins.[24]

3. Results

3.1. Verification of the hybrid structure

The solvothermal synthesis in this study yielded a dark yellow powder as the product (HNS-1DFe) with each particle in nanosheet form (see Fig. 1(a)). Details of this fundamental characterization are described in the SI (SI-1). The HNS-1DFe shows a flake-like morphology with a size of 1–5 μm. The thickness of HNS-1DFe can be estimated from Fig. 1(b) and is about 50–100 nm. Compositional analysis for HNS-1DFe revealed the minimum chemical composition as $Fe_7O_{4.77}(C_2H_4O_2)_9$. This result indicates the existence of an organic component, which is additionally verified by spectral analysis. Fig. 1(c) shows FT-IR and Raman spectra of HNS-1DFe and ethylene glycol (EG, $C_2H_6O_2$) used as the solvent during synthesis. Most of the peaks above 800 cm^{-1} for HNS-1DFe can be assigned to EG, while several fine structures with peak splitting and small shifts in wavenumber are also observed. The difference between the peaks of HNS-1DFe and

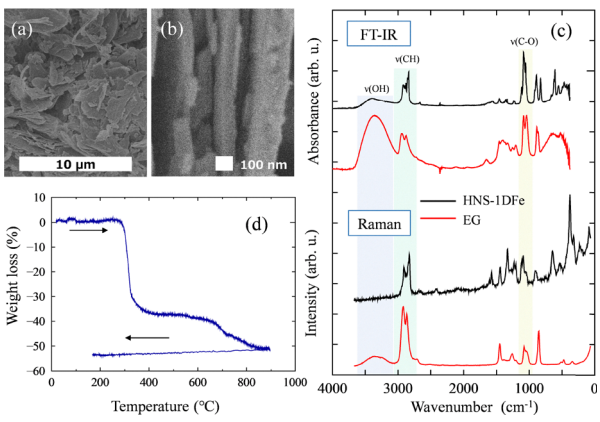

Fig. 1 Typical characteristics indicating a hybrid structured nanosheet for HNS-1DFe. (a) and (b) Typical SEM images. (c) Raman and FT-IR spectra. These spectra are compared with those of EG. (d) Weight loss measured by TG under heating and cooling procedures in N_2.

those of simple EG is attributed to the solidification of EG molecules.[25] For example, absorption bands at around 3700, 2900 and 1060 cm^{-1} are assigned to strong stretching modes of OH, CH, and C–O, respectively, in the case of liquid-state EG. However, the strong absorbance of the OH stretching-vibration at $\sim$3700 cm^{-1} is diminished in HNS-1DFe. This indicates that HNS-1DFe includes EG-derived organic molecules lacking hydrogen atoms.

Fig. 1(d) shows the weight loss of HNS-1DFe as a function of increasing and decreasing temperature. The weight loss starts at around 300 °C. This temperature is apparently higher than the boiling point of EG ($\approx$ 198 °C), and it defines the phase formation point of Fe_3O_4 from HNS-1DFe.[21] These observations lead to the conclusion that EG in HNS-1DFe does not exist as an adsorbed organic molecule but instead forms chemical bonds that allow its stabilization within the structure.

For characterizing the nanostructured matrix in HNS-1DFe, XAS and Mössbauer spectra were measured. The results are shown in Fig. 2. Fig. 2(a) compares the XANES spectrum of HNS-1DFe with those of α-Fe_2O_3 and $FeAl_2O_4$ measured as reference materials,[26] indicating Fe^{3+} and Fe^{2+}, respectively. Pre-edge peaks observed at around 7115 eV are due to 1s-to-3d forbidden transition of Fe K-edge absorption, and the position is almost the same for HNS-1DFe and α-Fe_2O_3. This peak position is known to depend on the valence state of iron ions.[27,28] Hence, these data indicate that the valence state of Fe in HNS-1DFe is similar to that in α-Fe_2O_3 rather than $FeAl_2O_4$. This trend is also identified from the absorption edge of XANES spectra. The absorption edge of HNS-1DFe is almost identical to that of α-Fe_2O_3, which shows that the valence state of Fe ions are all 3+ with the spin state, S = 5/2, in HNS-1DFe. Mössbauer spectra shown in Fig. 2(b) further support this observation; Fe^{2+} was not identified. Analysis details are given in SI (SI-2).

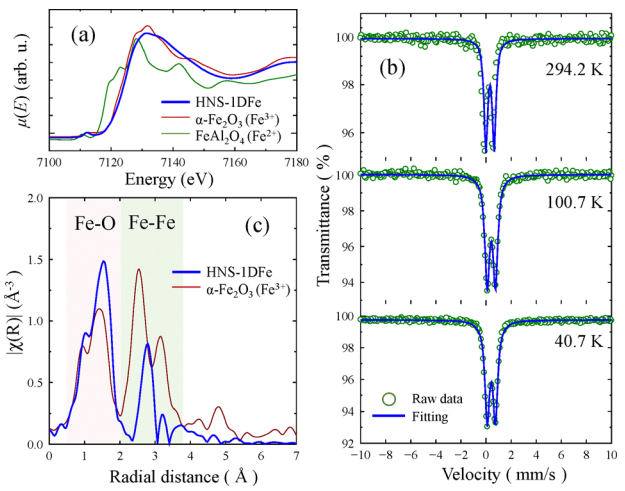

Fig. 2 Structural characteristics of HNS-1DFe. (a) XANES spectra of HNS-1DFe, α-Fe_2O_3 and $FeAl_2O_4$ as reference materials. (b) Mössbauer spectra measured at different temperatures. (c) Relationship between the radial distance and the radial distribution function calculated from XAS spectra.

Fig. 2(c) plots the radial distribution function against the radial distance with respect to the XAS spectra of Fe in HNS-1DFe and in that of α-Fe_2O_3. For α-Fe_2O_3, the origin of the first peaks (red area) is assigned to Fe–O distances (distances to the nearest-neighbour anions), and that of the second peaks (green area) is assigned to Fe–Fe distances (distances to the nearest-neighbour cations). This figure reveals that the radial distances of Fe–O bonds in α-Fe_2O_3 are almost the same as those between Fe and the nearest-neighbour-atom in HNS-1DFe, even though the densities differ. The average distance between Fe and its nearest-neighbour atoms is clearly shorter than the value in metallic iron ($\approx$2.5 Å)[29–31] and in iron-based complexes ($\approx$2.0 Å).[31–33] Therefore, the nanostructured matrix of HNS-1DFe is inferred to be an iron oxide.

3.2. Evaluation of low dimensionality of HNS-1DFe

Temperature dependence of the magnetic susceptibility, $\chi(T)$, of HNS-1DFe is presented in Fig. 3(a) (see also SI-3 in SI). The field-cooled (FC) $\chi(T)$, measured in a field of 10 kOe, shows a round maximum at $T_{max} \approx$ 120 K and a kink at around 21 K. The kink is indicative of a magnetic transition, while the broad maximum at higher temperature suggests magnetic order with low dimensionality of the spin system.[34] Therefore, we attempted to fit the data with 1D and 2D models for antiferromagnetic (AF) spin systems by applying the Fisher classical model[35] and the Lines model,[36] respectively, instead of the conventional Curie–Weiss law, which is established for 3D

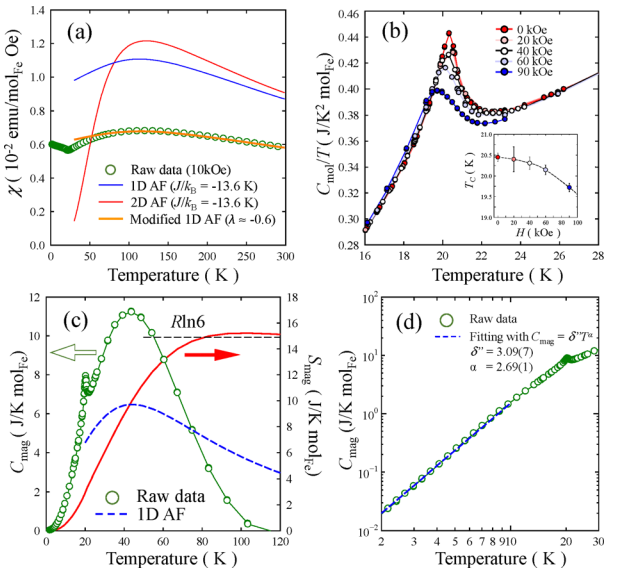

Fig. 3 Physical properties indicating low-dimensional spin system in HNS-1DFe. (a) Temperature dependence of normalized magnetic susceptibility for 1 mol of Fe^{3+} (S = 5/2). (b) Temperature dependence of the magnetic contribution of Fe^{3+} ions in the specific heat, divided by temperature, measured at various applied fields for HNS-1DFe. Inset shows the field variation of the maximum temperature indicated in the C_{mol}/T curves as T_C. (c) Temperature dependence of the magnetic contribution to the specific heat and the relationship between temperature and the magnetic entropy of HNS-1DFe at 0 Oe. (d) Logarithmic plot of the magnetic contribution in the specific heat used to fit a power law.

materials. For the Fisher classical model, $\chi(T)$ of a 1D AF material, $\chi_{1D}(T)$, was calculated from formulas (2) and (3).

$$\chi_{1D}(T) = \left[Ng^2{\mu_B}^2\frac{S(S+1)}{3k_BT}\right]\cdot\left[\frac{(1+u)}{(1-u)}\right] \quad (2)$$

$$u = \coth\left[\frac{2JS(S+1)}{k_BT}\right] - \frac{k_BT}{2JS(S+1)} \quad (3)$$

On the other hand, the Lines model calculates the $\chi(T)$ of 2D AF material, $\chi_{2D}(T)$, by formulas (4) and (5).

$$\chi_{2D}(T) = S(S+1)\left[\frac{Ng^2{\mu_B}^2}{3k_BT}\right] \times\left[1+\frac{A}{3\theta}+\frac{B}{3\theta^2}+\frac{C}{3\theta^3}+\frac{D}{3\theta^4}+\frac{E}{3\theta^5}+\frac{F}{3\theta^6}\right]^{-1} \quad (4)$$

$$\theta = \frac{k_BT}{JS(S+1)} \quad (5)$$

here, S = 5/2 (Fe^{3+}), g = 2, and the nearest-neighbour exchange interaction J/k_B is empirically determined as the fitting parameter. Then, A = 4, B = 1.448, C = 0.228, D = 0.262, E = 0.119, and F = 0.017 are used as the optimized parameters for S = 5/2.[36] Each fitting processes was conducted for the measured $\chi(T)$ as $\chi(T) = \chi_{1D}(T)$ and $\chi(T) = \chi_{2D}(T)$, respectively. Fig. 3(a) shows that the 1D model (blue line) provides a better fit than the 2D model (red line), even though a sizeable diamagnetic depression must be taken into account. Here, the value of J/k_B was determined as $J/k_B = -13.6$ K to fit the position of T_{max}. The magnitude of the diamagnetic shift for HNS-1DFe is quite large and cannot be explained by the influence of EG molecules. These fitting issues suggest the existence of an inter-chain interaction, J', between the 1D chains of the spin system, and the magnetism of HNS-1DFe is more precisely considered as quasi-1D antiferromagnetism. Therefore, we considered the influence of J' for fitting the data of $\chi(T)$. Here, $\chi(T)$ was taken as the origin of the magnetism of the sample, and M and H were defined as the magnetization of the sample and the applied magnetic field, respectively. That is, $\chi(T) = M/H$. On the other hand, $\chi_{1D}(T)$ is considered to be the response to the effective magnetic field, $H + \lambda M$. Here, λ is the molecular field coefficient including the contribution of J', and it is expected to be $\lambda \neq 0$ in the case of $J' \neq 0$. In this case, $\chi_{1D}(T)$ is expressed as $\chi_{1D}(T) = M/(H + \lambda M)$. These two equations give rise to formula (6).

$$\chi(T) = \frac{\chi_{1D}(T)}{1-\lambda\chi_{1D}(T)} \quad (6)$$

Fig. 3(a) shows the successful fit by the modified 1D model (orange line) obtained by applying formula (6) with $\lambda \approx -0.6$ to $\chi_{1D}(T)$ with $J/k_B = -13.6$ K. These results indicate quasi-1D antiferromagnetism with the contribution of J' in HNS-1DFe.

Low dimensionality of the spin system in HNS-1DFe was also verified by heat capacity measurements. First, Fig. 3(b) shows the specific heat divided by temperature, C_{mol}/T. A small peak appears at 20.4 K, corresponding to the critical transition temperature, T_C, in Fig. 3(a). This peak temperature is slightly depressed by applying a magnetic field (see the inset in Fig. 3(b)). Next, the magnetic contribution of Fe^{3+} ions to the specific heat, C_{mag}, is plotted in Fig. 3(c). Remarkably, $C_{mag}(T)$ exhibits a broad maximum at $T_{max} \approx 44$ K above the magnetic transition at T_C. This indicates that the magnetic degrees of freedom of Fe^{3+} ions persist at high temperatures, $T \gg T_C$. Thus, the existence of strong AF spin correlations or low-dimensional spin fluctuations in the spin system is considered the origin of the broad maximum in $C_{mag}(T)$. This point is verified by a theoretical calculation for the 1D AF spin system,[38] and the computed line is drawn (bold dashed blue line) in Fig. 3(c). Here, theoretical calculations reproduce draw the $C_{mag}(T)$ behaviour using formulas (7) and (8). Then, a_2 = 11.097, a_2 = 11.097, a_3 = −0.8511, a_4 = 0.1799, b_1 = 0.0195, b_2 = 0.5845, and γ = 1.8081 are used as the optimized parameters for S = 5/2.[37]

$$C_{mag}(T) = \frac{a_2K^2 + a_3K^3 + a_4K^4}{(1+b_1K+b_2K^2)^{\gamma}} \quad (7)$$

$$K = \frac{JS(S+1)}{k_BT} \quad (8)$$

The model curve does not represent the experimental curve well, and this discrepancy is attributed to the existence of J' between the 1D chains of the spin system in HNS-1DFe.

The magnetic entropy, $S_{mag}(T)$, is also plotted in Fig. 3(c). It is worth noting that $S_{mag}(T)$ reaches a saturation value of S_{mag} = 15 J K^{-1} $mol_{Fe}{}^{-1}$ at temperatures as high as T = 100 K, which corresponds well to the theoretically expected value of $S_{spin} = Rln(2S+1)$ = 14.9 J K^{-1} $mol_{Fe}{}^{-1}$ for S = 5/2. This is consistent with the previous results.

On the other hand, the kink at 21 K is remarkable because such a transition phenomenon is not expected for a typical 1D AF spin system.[38] This is further evidence of the intrinsic quasi-1D characteristics of the spin system in HNS-1DFe. The $C_{mag}(T)$ at $T \ll T_C$ is expected to follow a cubic power law, $C_{mag} = \delta'' T^{\alpha}$ ($\alpha \approx 3$).[24] In our case, $C_{mag}(T)$ follows the power law $C_{mag} = \delta'' T^{2.69(1)}$ with δ'' = 3.09(7) mJ $K^{-2.69}$ below 10 K (Fig. 3(d)). The theoretical exponent is discussed as d_{mag}/n,[24] where d_{mag} is the dimension of the spin system and n is an index indicating ferromagnetic (n = 2) or AF (n = 1) interactions between spins. That is, the exponent value of a ferromagnetic spin system should be 0.5–1.5 and that of a 3D AF system should be ≈3. An exponent value of 2.69(1) is much higher than 1.5 and clearly lower than 3. This result is in-line with a low-dimensional AF systems with the existence of J' in the low-temperature phase of HNS-1DFe.

3.3. Structural characterization of HNS-1DFe

Experimental details and the raw data are presented in SI (SI-5). In Fig. 4(a), the XRD and PND patterns of HNS-1DFe are plotted against the lattice distance, d. This figure truncates the extremely intense peak observed at $d \approx 8.05$ Å in order to focus on other small peaks. There are several sharp peaks in the XRD pattern, which can be assigned to fractional numbers of the

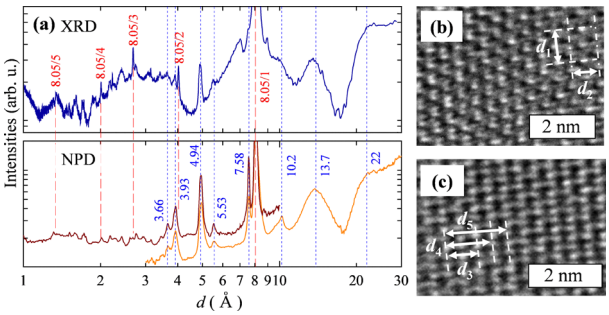

Fig. 4 Structural information relating to the 1D iron oxide matrix in HNS-1DFe. (a) Diffraction patterns plotted against lattice distance, *d*, of XRD and PND measurements for HNS-1DFe. The PND measurement yielded two patterns corresponding to different detector set points, enabling collection of a wide range of diffraction data. (b) Typical high-resolution images observed by TEM of the nanosheet surface. (c) TEM image observed in the vicinity of the typical images shown in (b).

main intense peak considered to originate from the iron oxide matrix (see the red line in Fig. 4(a)). This series of peaks can be indexed as 00*l*, with a lattice constant of ≈8.05 Å. On the other hand, both diffraction patterns display many broad peaks that can be attributed to the organic molecules in HNS-1DFe. However, assignment of these peaks is not as easy as that of the 00*l* peaks; hence, HNS-1DFe appears to belong to a crystal system with an axial angle ≠90°. Fig. 4(a) shows the position of these typical peaks to clarify the characteristic distances in HNS-1DFe.

The nanosheet surface of HNS-1DFe was studied by TEM observation. The most frequently observed surface area is shown in Fig. 4(b), while Fig. 4(c) and the mesophases (speculated) between them were also observed in the surrounding regions. Gerber *et al.* reported a hybrid nanosheet of 1D iron oxide synthesized under similar conditions to those used for HNS-1DFe.[39] Their hybrid nanosheet configures zebra array structure, in which organic molecules and 1D iron oxide align alternately along the nanosheet surface. However, our TEM observation couldn't find this zebra array structure for HNS-1DFe. Instead, Fig. 4(b), which is a typical TEM image of HNS-1DFe, shows a hexagonal arrangement of atoms, where the observed atoms are considered to be Fe. The symbolic lengths described in Fig. 4(b) as d_1 and d_2 are estimated as 10 and 8 Å, respectively. (Note that it cannot be concluded that these lengths correspond to 8.05 Å and 10.2 Å, obtained from XRD and PND data. The atomic planes with $d \approx 8$ Å have another atomic plane between them, which will scatter in anti-phase, making the intensity of the reflection at 8 Å zero.) In this case, the distance between two Fe atoms was about 5 Å, significantly longer than the typical distance (<4 Å) in iron oxides. Additionally, it is much longer than the calculated radial distance extracted from Fig. 2(c) (≈2.8 Å).

On the other hand, we were able to observe other views for HNS-1DFe. Fig. 4(c) shows that atoms form short-bond stacking while sliding their positions uniformly. In that case, distances of 8 Å, 14 Å, and 20 Å (≈8.05 Å, ≈13.7 Å, and <22 Å) corresponding to d_3, d_4, and d_5 drawn in Fig. 4(c), respectively. This image is considered to relate to the periodicity of the 1D iron oxide chain.

4. Discussion

4.1. Low-dimensional structure of iron oxide

In the previous sections we have demonstrated that the spin system in HNS-1DFe orders with a quasi-1D nature. This is attributed to the magnetic moments of Fe^{3+} in the iron oxide matrix. Magnetism in transition-metal oxides is usually mediated by superexchange interaction; hence a 1D (or quasi-1D) network of the chemical bonds between Fe^{3+} and O^{2-} should structurally exist in HNS-1DFe. However, this does not directly indicate the structural low dimensionality of iron oxide matrix in HNS-1DFe. This section discusses the structural low dimensionality of HNS-1DFe in more detail.

This low dimensionality of iron oxide in HNS-1DFe is inferred from the Mössbauer data described in SI (SI-2). Here, the isomer shift, δ, of Fe^{3+} is relatively small (=0.316 mm s^{-1} at 294.2 K) compared to the typical value for Fe^{3+}-based oxides. Based on the general understanding of the analysis of ^{57}Fe Mössbauer spectra for 3D materials, this small δ suggests that Fe^{3+} in HNS-1DFe locally has a tetrahedral coordination rather than an octahedral one. However, this is not common for simple Fe^{3+} oxides. In contrast, the small δ value is reasonable if the iron oxide matrix has a low-dimensional configuration with a relatively small number of surrounding anions. This result indicates the structural low dimensionality of iron oxide in HNS-1DFe, since the origin of the magnetism is only Fe^{3+} in the case of this material. The Debye temperature, Θ_D, calculated from the Mössbauer spectra also implies this trend. The calculated Θ_D of HNS-1DFe is 245 K, consistent with the value Θ_D = 237 K obtained from the fitting process of C_{mol} (see SI SI-2 and SI-4). These Θ_D values are smaller than those of Fe_2O_3 (300–330 K)[40] and suggest weaker bonds around Fe^{3+} in HNS-1DFe than those in Fe_2O_3 with a 3D structure.

On the other hand, Fig. 2(c) shows that the density of the distances to the nearest-neighbour cation (assigned as Fe–Fe distances) of Fe^{3+} in HNS-1DFe is smaller than that in α-Fe_2O_3. This indicates that the number of surrounding ions is relatively small in the case of Fe^{3+} in HNS-1DFe. This observation is in agreement with the structural low dimensionality of the iron oxide matrix in HNS-1DFe.

From these data, we consider that the magnetic low dimensionality of HNS-1DFe is strongly correlated with the structural uniqueness of the 1D iron oxide matrix.

4.2. Quasi-1D structure of iron oxide

The preceding section argues for the structural uniqueness of the 1D iron oxide matrix in HNS-1DFe. In general, a 1D network is assumed to be a continuous straight chain structure, and thus of the term "chain" is used to describe the 1D network for clarity. However, some experimental data of HNS-1DFe indicate the contribution of J' to overall 1D magnetism. This requires further structural verification for the 1D network of Fe^{3+} and

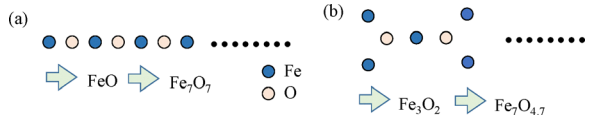

Fig. 5 Simplified model of the 1D iron oxide structure in HNS-1DFe. (a) Continuous straight chain model. (b) Modified model with Fe_3O_2 composition.

O^{2-}. Therefore, this section examines the structure of the 1D network.

The simplest structural model for the 1D iron oxide is a continuous straight chain (see the illustration in Fig. 5(a)). However, Fig. 2(c) indicates that the average distance between Fe^{3+} and O^{2-} is about 1.55 Å. Then, the average distance between Fe^{3+} and Fe^{3+} is about 2.8 Å. Therefore, if one calculates a bond angle of Fe–O–Fe bonds, it is about 129°. This indicates that the 1D iron oxide in HNS-1DFe is not a straight chain like that shown in Fig. 5(a) but instead has at least a zigzag structure. Additionally, the chemical composition of HNS-1DFe would be expected to be $Fe_7O_7(C_2H_4O_2)_9$ in the case of a simple continuous chain. However, the oxygen content of the 1D iron oxide in HNS-1DFe is calculated as 4.77, which is considered smaller than expected. The oxygen content was not directly measured, and thus the accuracy is limited. There is the possibility that the residual oxygen content is 7 if we measured it exactly. However, further evidence for a residual oxygen content of 4.7 comes from considering the isolated 1D iron oxides in the inorganic–organic hybrid structure. For example, atomic ordering as shown in Fig. 5(b) may generate quasi-1D iron oxide with some magnetic frustration, and the chemical composition becomes Fe_3O_2. The chemical composition of Fe_3O_2 can correspond to $Fe_7O_{4.7}$ if the Fe content is calculated as 7, taking into account $Fe_7O_{4.77}(C_2H_4O_2)_9$ as the minimum chemical composition of HNS-1DFe. This possibility is therefore also reasonable for explaining the origin of the phase transition phenomenon at $T_C \approx 21$ K, since the quasi-1D iron oxide structure is expected to be more rigid than a simple chain. Fig. 5(b) is a 2D image drawn with 120° of Fe–O–Fe bonds, and HNS-1DFe involves organic molecules of EG in the hybrid structure; therefore, the real crystal structure is considered more complex. However, this speculation implies the possibility that the 1D iron oxides in HNS-1DFe form a quasi-1D structure rather than simple zigzag chains.

5. Summary

This investigation reports the discovery of HNS-1DFe as a novel hybrid nanosheet. Interestingly, the spin system of this material shows quasi-1D magnetism. This characteristic property was carefully verified through several experiments performed independently, and the obtained results were all consistent with the proposed structural model.

Notably, the results indicate that the iron oxide matrix in HNS-1DFe has the potential to give rise to a phase-transition phenomenon, since its quasi-1D structure is expected to be more rigid than a simple 1D straight chain. Transition-metal oxides are widely known as effective platforms for investigating novel functional materials. Therefore, the rigid structure of iron oxide in HNS-1DFe is expected to pave the way for tailoring low-dimensional functional properties. HNS-1DFe is a hybrid nanomaterial, and the hybrid nanomaterial has an advantage for controlling the overall structure by arranging the organic molecules. The potential for tailoring novel functional devices using this nanosheet warrants a future detailed investigation of HNS-1DFe.

Author contributions

The manuscript was written through the contributions of all authors. T. Nakane, T. Naka and HA contributed equally to this work. Material preparations were performed by HA. Fundamental evaluations were exhibited by HA, T. Nakane and KS. Structural characterization and the analysis were exhibited by T. Nakane, NT, DDK and PM. Measurement of XAS spectra and the analysis was performed by CN and T. Naka. On the other hand, evaluation of the magnetism and the analysis was conducted by T. Naka and T. Nakane. Specific heat measurement and the analysis was exhibited and analysed by T. Naka and AdV. Mössbauer spectra were collected and analysed by AI and SK. Finally, all authors have approved the final version of the manuscript.

Conflicts of interest

The authors declare that they have no competing interest.

Data availability

All relevant data are within the manuscript and supplementary information (SI). Supplementary information is available. See DOI: https://doi.org/10.1039/d5tc03791c.

Acknowledgements

This work was supported by a Grant-in-Aid for the Cooperative Research Project of Design & Engineering by Joint Inverse Innovation for Materials Architecture (DEJI^{2}MA) of the Ministry of Education, Culture, Sports, Science and Technology (MEXT), and JSPS KAKENHI Grant Number (21H01637, 16K13999 and 24K08507). This work was conducted with experimental supports of the NIMS Electron Microscopy Unit and the NIMS Surface and Bulk Analysis Unit.

References

1 D. Jérome, A. Mazaud, M. Ribault and K. Bechgaard, Superconductivity in a synthetic organic conductor $(TMTSF)_2PF_6$, *J. Phys., Lett.*, 1980, **41**, L95–L98.
2 M. Fujioka, M. Jeem, K. Sato, M. Tanaka, K. Morita, T. Shibuya, K. Takahashi, S. Iwasaki, A. Miura, M. Nagao,

S. Demura, H. Sakata, M. Ono, H. Kaiju and J. Nishii, Intercalation on Transition Metal Trichalcogenides via a Quasi-Amorphous Phase with 1D Order, *Adv. Funct. Mater.*, 2023, **33**, 2208702.

3 F. Kagawa, T. Itou, K. Miyagawa and K. Kanoda, Transport criticality of the first-order Mott transition in the quasi-two-dimensional organic conductor k-(BEDT-TTF)$_2$Cu[N(CN)$_2$]Cl, *Phys. Rev. B: Condens. Matter Mater. Phys.*, 2004, **69**, 64511.

4 Y. Shimizu, K. Miyagawa, K. Kanoda, M. Maesato and G. Saito, Spin Liquid State in an Organic Mott Insulator with a Triangular Lattice, *Phys. Rev. Lett.*, 2003, **91**, 107001.

5 A. Ishii and A. Miyasaka, A. Direct detection of circular polarized light in helical 1D perovskite-based photodiode, *Sci. Adv.*, 2020, **6**, eabd3274.

6 A. F. Santander-Syro, O. Copie, T. Kondo, F. Fortuna, S. Pailhès, R. Weht, X. G. Qiu, F. Bertran, A. Nicolaou, A. Taleb-Ibrahimi, P. Le Fèvre, G. Herranz, M. Bibes, N. Reyren, Y. Apertet, P. Lecoeur, A. Barthélémy and M. J. Rozenberg, Two-dimensional electron gas with universal subbands at the surface of $SrTiO_3$, *Nature*, 2011, **469**, 189–193.

7 S. Iijima, Helical microtubules of graphitic carbon, *Nature*, 1991, **354**, 56–58.

8 H. Ishii, H. Kataura, H. Shiozawa, H. Yoshioka, H. Otsubo, Y. Takayama, T. Miyahara, S. Suzuki, Y. Achiba, M. Nakatake, T. Narimura, M. Higashiguchi, K. Shimada, H. Namatame and M. Taniguchi, Direct observation of Tomonaga–Luttinger-liquid state in carbon nanotubes at low temperatures, *Nature*, 2003, **426**, 540–544.

9 A. K. Geim and K. S. Novoselov, The Rise of Graphene, *Nat. Mater.*, 2007, **6**, 183–191.

10 S. Tomonaga, Remarks on Bloch's Method of Sound Waves applied to Many-Fermion Problems, *Prog. Theor. Phys.*, 1950, **5**, 544–569.

11 J. M. Luttinger, An Exactly Soluble Model of a Many-Fermion System, *J. Math. Phys.*, 1963, **4**, 1154–1162.

12 D. C. Mattis and E. H. Lieb, Exact Solution of a Many-Fermion System and Its Associated Boson Field, *J. Math. Phys.*, 1965, **6**, 304–312.

13 F. D. M. Haldane, Continuum dynamics of the 1-D Heisenberg antiferromagnet: Identification with the O(3) nonlinear Sigma model, *Phys. Lett. A*, 1983, **93**, 464–468.

14 F. D. M. Haldane, Nonlinear Field Theory of Large-Spin Heisenberg Antiferromagnets: Semiclassically Quantized Solitons of the One-Dimensional Easy-Axis Néel State, *Phys. Rev. Lett.*, 1983, **50**, 1153–1156.

15 A. Kojima, K. Teshima, Y. Shirai and T. Miyasaka, Organometal Halide Perovskites as Visible-Light Sensitizers for Photovoltaic Cells, *J. Am. Chem. Soc.*, 2009, **131**, 6050–6051.

16 M. G. Yamada, H. Fujita and M. Oshikawa, Designing Kitaev Spin Liquids in Metal-Organic Frameworks, *Phys. Rev. Lett.*, 2017, **119**, 057202.

17 T. Takenaka, K. Ishihara, M. Roppongi, Y. Miao, Y. Mizukami, T. Makita, J. Tsurumi, S. Watanabe, J. Takeya, M. Yamashita, K. Torizuka, Y. Uwatoko, T. Sasaki, X. Huang, W. Xu, D. Zhu, N. Su, J. G. Cheng, T. Shibauchi and K. Hashimoto, Strongly correlated superconductivity in a copper-based metal-organic framework with a perfect kagome lattice, *Sci. Adv.*, 2021, **7**, eabf3996.

18 K. Wang, L. Jin, Y. Gao, A. Liang, B. P. Finkenauer, W. Zhao, Z. Wei, C. Zhu, T. F. Guo, L. Huang and L. Dou, Lead-Free Organic−Perovskite Hybrid Quantum Wells for Highly Stable Light-Emitting Diodes, *ACS Nano*, 2021, **15**, 6316–6325.

19 M. Kondo, T. Yoshitomi, K. Seki, H. Matsuzaka and S. Kitagawa, Three-Dimensional Framework with Channeling Cavities for Small Molecules: {[M2(4, 4'-bpy)$_3$(NO$_3$)$_4$]·xH$_2$O}n (M = Co, Ni, Zn), *Angew. Chem., Int. Ed. Engl.*, 1997, **36**, 1725–1727.

20 H. Li, M. Eddaoudi, T. L. Groy and O. M. Yaghi, Establishing Microporosity in Open Metal−Organic Frameworks: Gas Sorption Isotherms for Zn(BDC) (BDC = 1,4-Benzenedicarboxylate), *J. Am. Chem. Soc.*, 1998, **120**, 8571–8572.

21 H. Abe, T. Naka, K. Sato, K. Suzuki and M. Nakano, Shape-Controlled Syntheses of Magnetite Microparticles and Their Magnetorheology, *Int. J. Mol. Sci.*, 2019, **20**, 3617–3627.

22 L. C. Chapon, P. Manuel, P. G. Radaelli, C. Benson, L. Perrott, S. Ansell, N. J. Rhodes, D. Raspino, D. Duxbury, E. Spill and J. Norris, Wish: The new powder and single crystal magnetic diffractometer on the second target station, *Neutron News*, 2011, **22**, 22–25.

23 B. Ravel and M. Newville, ATHENA, ARTEMIS, HEPHAESTUS: data analysis for X-ray absorption spectroscopy using IFEFFIT, *J. Synchrotron. Rad.*, 2005, **12**, 537–541.

24 L. J. de Jongh and A. R. Miedema, Experiments on simple magnetic model systems, *Adv. Phys.*, 1974, **23**, 1–260.

25 K. Krishman and R. S. Krishman, Raman and Infrared Spectra of Ethylene Glycol, *Proc. Indian Acad. Sci. Sect. A*, 1966, **64**, 111–122.

26 T. Nakane, S. Ishii, T. Naka and T. Uchikoshi, Influence of Fabrication Conditions on the Structural Characteristics and the Magnetic Properties of $FeAl_2O_4$, *J. Am. Ceram. Soc.*, 2023, **106**, 2317–2325.

27 M. Wilke, F. Farges, P.-E. Petit, G. E. Brown and F. Martin, Oxidation state and coordination of Fe in minerals: An Fe *K*-XANES spectroscopic study, *Am. Mineral.*, 2001, **86**, 714–730.

28 R. Murao, T. Harano, M. Kimura and I.-H. Jung, Thermodynamic Modeling of the SFCA Phase $Ca_2(Fe,Ca)_6(Fe,Al,Si)_6O_{20}$, *ISIJ Int.*, 2018, **58**, 259–266.

29 N. V. Ershov, Y. A. Babanov and V. R. Galakhov, EXAFS Study of Crystalline Cu, Ni, and Fe, *Phys. Stat. Solidi B*, 1983, **117**, 749–753.

30 P. Srivastava, L. Lemke, H. Wende, R. Chauvistré, N. Haack, K. Baberschke, J. Hunter-Dunn, D. Arvanitis, N. Mårtensson, A. Ankudinov and J. J. Rehr, Magnetic extended x-ray absorption fine structure at the $L_{3,2}$ edges of Fe and Co on Cu(001), *J. Appl. Phys.*, 1998, **83**, 7025–7027.

31 N. Parsai and A. Mishra, Study of XAFS of some Fe compounds and determination of first shell radial distance, *J. Phys.: Conf. Ser.*, 1998, **836**, 012045.

32 V. G. Vlasenko, A. T. Shuvaev, T. I. Nedoseikina, A. L. Nivorozhkin, A. I. Uraev, A. D. Garnovskii and O. Y. Korshunov, EXAFS studies of the novel iron(III) complexes with an N/S(Se) chromophore simulating ligand

environment of the active site of nitrile hydratase, *J. Synchrotron Rad.*, 1999, **6**, 406–408.

33 Y. T. Chen, K. H. C. Chen and M. Fukuda, DFT Study for Evaluation of the Interraction of Coordinated Molecule to Fe(III) in Various Iron(III)Chloride Complexes, *J. Comput. Chem. Jpn.*, 2017, **16**, 1–16.

34 H. Lu, T. Yamamoto, W. Yoshimune, N. Hayashi, Y. Kobayashi, Y. Ajiro and H. A. Kageyama, Nearly Ideal One-Dimensional S = 5/2 Antiferromagnet FeF_3(4,4-bpy) (4,4-bpy =4,4-bipyridyl) with Strong Intrachain Interactions, *J. Am. Chem. Soc.*, 2015, **137**, 9804–9807.

35 M. E. Fisher, Magnetism in One-Dimensional Systems - The Heisenberg Model for Infinite Spin, *Am. J. Phys.*, 1964, **32**, 343–346.

36 M. E. Lines, The quadratic-layer antiferromagnet, *J. Phys. Chem. Solids*, 1970, **31**, 101–116.

37 T. de Neef, A. J. M. Kuipers and K. Kopinga, Magnetic specific heat of isotropic linear chains for $S \leqslant 5/2$, *J. Phys. A: Math., Nucl. Gen.*, 1974, **7**, L171–L175.

38 E. Ijing, Beitrag zur Theorie des Ferromagnetismus, *Z. Phys.*, 1925, **31**, 253–258.

39 O. Gerber, B. P. Pichon, D. Ihiawakrim, I. Florea, S. Moldovan, O. Ersen, D. Begin, J.-M. Grenèche, S. Lemonnier, E. Barraud and S. Begin-Colin, Synthesis engineering of iron oxide raspberry-shaped nanostructures, *Nanoscale*, 2017, **9**, 305–313.

40 A. Ibrahim, K. Tani, K. Hashi, B. Zhang, Z. Homonnay, E. Kuzmann, A. Bafti, L. Pavić, S. Krehula, M. Marciuš and S. Kubuki, Debye Temperature Evaluation for Secondary Battery Cathode of α-$Sn_xFe_{1-x}OOH$ Nanoparticles Derived from the 57Fe- and 119Sn-Mössbauer Spectra, *Int. J. Mol. Sci.*, 2024, **25**, 2488–2513.